

# Geophysical Research Letters

## RESEARCH LETTER

10.1029/2020GL091585

### Key Points:

- Observed instantaneous radiative forcing has increased, strengthening the top-of-atmosphere radiative imbalance
- Due to cancellations in longwave and shortwave radiation, the sum of rapid adjustments and radiative feedbacks exhibit an insignificant trend
- Observed increases in instantaneous radiative forcing are direct evidence of the anthropogenic effects on the Earth's radiative energy budget

### Supporting Information:

Supporting Information may be found in the online version of this article.

### Correspondence to:

R. J. Kramer,  
[ryan.j.kramer@nasa.gov](mailto:ryan.j.kramer@nasa.gov)

### Citation:

Kramer, R. J., He, H., Soden, B. J., Oreopoulos, L., Myhre, G., Forster, P. M., & Smith, C. J. (2021). Observational evidence of increasing global radiative forcing. *Geophysical Research Letters*, 48, e2020GL091585. <https://doi.org/10.1029/2020GL091585>

Received 5 NOV 2020

Accepted 11 MAR 2021

## Observational Evidence of Increasing Global Radiative Forcing

Ryan J. Kramer<sup>1,2</sup> , Haozhe He<sup>3</sup>, Brian J. Soden<sup>3</sup> , Lazaros Oreopoulos<sup>1</sup> , Gunnar Myhre<sup>4</sup> , Piers M. Forster<sup>5</sup> , and Christopher J. Smith<sup>5,6</sup> 

<sup>1</sup>NASA Goddard Space Flight Center, Earth Sciences Division, Greenbelt, MD, USA, <sup>2</sup>Universities Space Research Association, Columbia, MD, USA, <sup>3</sup>Rosenstiel School of Marine and Atmospheric Science, University of Miami, Miami, FL, USA, <sup>4</sup>CICERO Center for International Climate and Environmental Research in Oslo, Oslo, Norway, <sup>5</sup>School of Earth and Environment, University of Leeds, Leeds, UK, <sup>6</sup>International Institute for Applied Systems Analysis (IIASA), Laxenburg, Austria

**Abstract** Changes in atmospheric composition, such as increasing greenhouse gases, cause an initial radiative imbalance to the climate system, quantified as the instantaneous radiative forcing. This fundamental metric has not been directly observed globally and previous estimates have come from models. In part, this is because current space-based instruments cannot distinguish the instantaneous radiative forcing from the climate's radiative response. We apply radiative kernels to satellite observations to disentangle these components and find all-sky instantaneous radiative forcing has increased  $0.53 \pm 0.11 \text{ W/m}^2$  from 2003 to 2018, accounting for positive trends in the total planetary radiative imbalance. This increase has been due to a combination of rising concentrations of well-mixed greenhouse gases and recent reductions in aerosol emissions. These results highlight distinct fingerprints of anthropogenic activity in Earth's changing energy budget, which we find observations can detect within 4 years.

**Plain Language Summary** Climate change is a response to energy imbalances in the climate system. For example, rising greenhouse gases directly cause an initial imbalance, the radiative forcing, in the planetary radiation budget, and surface temperatures increase in response as the climate attempts to restore balance. The radiative forcing and subsequent radiative feedbacks dictate the amount of warming. While there are well-established observational records of greenhouse gas concentrations and surface temperatures, there is not yet a global measure of the radiative forcing, in part because current satellite observations of Earth's radiation only measure the sum total of radiation changes that occur. We use the radiative kernel technique to isolate radiative forcing from total radiative changes and find it has increased from 2003 to 2018, accounting for nearly all of the long-term growth in the total top-of-atmosphere radiation imbalance during this period. We confirm that rising greenhouse gas concentrations account for most of the increases in the radiative forcing, along with reductions in reflective aerosols. This serves as direct evidence that anthropogenic activity has affected Earth's energy budget in the recent past.

## 1. Introduction

The Instantaneous Radiative forcing (IRF) is the initial imbalance of the Earth's top-of-the-atmosphere (TOA) radiative energy budget directly caused by a change in atmospheric composition, such as increasing greenhouse gases (GHGs), or perturbed surface properties, like from land use change. All anthropogenic climate changes are a response to the IRF, including surface temperature change and associated radiative feedbacks (Sherwood et al., 2015). Despite a sound basis in physics and radiative transfer theory, the IRF is hard to directly diagnose from observations. Multiple remote sensing and in-situ instruments observe net radiative fluxes, but these measurements convolve the IRF with radiative responses to the changing atmospheric state. Some studies have diagnosed a more broadly defined "greenhouse effect" by evaluating observations of clear-sky longwave radiation at the surface (Philipona et al., 2004) and TOA (Raghuraman et al., 2019), but this analysis does not separate the IRF from water vapor feedback processes.

Harries et al. (2001) compared outgoing longwave radiation at the TOA from two satellite instruments launched decades apart, attributing emission differences at relevant spectral bands to rising greenhouse

gas (GHG) concentrations. However, instrumental uncertainty between the two platforms complicates interpretation (Jiang et al., 2011). Feldman et al. (2015, 2018) used ground observations from the US Department of Energy Atmospheric Radiation Measurement program to provide the most observationally oriented assessment to date of GHG surface radiative forcing, which is proportional to the TOA IRF. However, their analysis was limited to longwave (LW) forcing from CO<sub>2</sub> and CH<sub>4</sub> and was only conducted for two locations. The total IRF has not been directly diagnosed globally from observations.

Well understood radiative transfer theory tightly constraints the GHG component of the IRF. Line-by-line radiative transfer models diagnose it within 1% agreement (Collins et al., 2006; Mlynchzak et al., 2016; Pincus et al., 2020). However, these highly accurate calculations are computationally expensive, so analysis is often limited to a few idealized atmospheric profiles. Quantifying the IRF globally and over time relies on more efficient but less accurate parameterized radiative transfer models (Soden et al., 2018), which introduces model bias when applied to observations. Diagnosing the IRF from aerosols with these models suffers from the same pitfalls, plus additional uncertainty associated with aerosol optical properties that are not well-observed (Randles et al., 2013; Stier et al., 2013). While there have been recent efforts to constrain aerosol IRF with observations (Bellouin et al., 2020; Watson-Parris et al., 2020), results are usually not temporally resolved.

Here, we circumvent these limitations by applying radiative kernels (Soden et al., 2008) to isolate the IRF from radiative feedbacks and rapid adjustments over time. We demonstrate that the IRF has increased with rising GHG concentrations, accounting for recent, positive trends in the total TOA radiative imbalance. More specifically, we consider this IRF to be largely a consequence of concentration changes after anthropogenic emissions are moderated by natural carbon cycle responses (Friedlingstein et al., 2019).

## 2. Methods

Variations in the total, all-sky radiative energy balance at the TOA,  $dR$ , constrain global surface temperature change and consists of the all-sky IRF and radiative responses to the IRF:

$$dR = \text{IRF} + dR_{\lambda}, \quad (1)$$

where  $dR_{\lambda}$  is the net radiative changes caused by surface temperature-mediated radiative feedbacks and rapid adjustments from, to first order, temperature ( $T$ ), water vapor ( $q$ ), surface albedo ( $\alpha$ ) and cloud ( $C$ ) changes (Sherwood et al., 2015; Vial et al., 2013):

$$dR_{\lambda} = dR_T + dR_q + dR_{\alpha} + dR_C. \quad (2)$$

For simplicity, we will not decompose these terms further into feedbacks and rapid adjustments since it has no bearing on diagnosing the IRF. We simply refer to these radiative anomalies as radiative responses. We note that  $dR_{\lambda}$  includes both anthropogenic responses and natural variability (e.g., Trenberth et al., 2015).

The Clouds and Earth's Radiant Energy System (CERES) has provided global TOA energy balance observations since 2000. Here, we diagnose  $dR$  using radiative flux anomalies from the CERES Energy Balance and Filled (EBAF) Ed. 4.1 product (Loeb et al., 2018b; Loeb et al., 2019). While no observational product measures the radiative response terms in isolation, they can be diagnosed using radiative kernels combined with observations of the relevant state variable,  $x$  (B. Zhang et al., 2019; Bony et al., 2020). An individual, non-cloud radiative response,  $dR_x$ , in linear form is:

$$dR_x = \frac{\partial R}{\partial x} dx = K_x dx, \quad x = T, q, \alpha, \quad (3)$$

where  $K_x$  is a radiative kernel representing direct radiative changes from small, standard perturbations in state variable  $x$  and  $dx$  is the actual temperature ( $T$ ), water vapor ( $q$ ) or surface albedo ( $\alpha$ ) climate response. Under clear-sky (CS) conditions:

$$dR^{\text{CS}} = \text{IRF}^{\text{CS}} + dR_{\lambda}^{\text{CS}}, \quad (4)$$

where:

$$dR_{\lambda}^{\text{CS}} = dR_T^{\text{CS}} + dR_q^{\text{CS}} + dR_{\alpha}^{\text{CS}}. \quad (5)$$

To diagnose  $dR_x$  or  $dR_x^{\text{CS}}$ , we use observational-based radiative kernels developed from the CloudSat Fluxes and Heating Rates product 2B-FLXHR-LIDAR (Kramer et al., 2019). Unlike GCM-derived radiative kernels, these kernels are free from model bias in the base state, and thus ideal for diagnosing observed radiation changes. Calculating  $K_x$  requires using a radiative transfer model to convert base state perturbations to radiative sensitivities. Therefore, using radiative kernels introduces some radiative-transfer model dependency. We apply the radiative kernels to deseasonalized anomalies of temperature and specific humidity profiles from version 6 Level 3 AIRS retrievals (Aumann et al., 2003) to estimate  $dR_T$  and  $dR_q$  and to surface albedo anomalies from CERES EBAF surface fluxes (Kato et al., 2018) to estimate  $dR_{\alpha}$ . Due to computational expense, radiative kernels, including those used here, are often derived from one year of data. However radiative kernel inter-annual variability is small (Pendergrass et al., 2018; Thorsen et al., 2018), therefore applying radiative kernels to the entire observational record is justified.

In the traditional radiative kernel technique used here, the cloud radiative response ( $dR_C$ ) is calculated as the change in cloud radiative effects (CRE) corrected for cloud masking (Kramer et al., 2019; Soden et al., 2008):

$$dR_C = d\text{CRE} - \left( dR_T - dR_T^{\text{CS}} \right) - \left( dR_q - dR_q^{\text{CS}} \right) - \left( dR_{\alpha} - dR_{\alpha}^{\text{CS}} \right) - \left( \text{IRF} - \text{IRF}^{\text{CS}} \right), \quad (6)$$

where CRE is the difference between all-sky and clear-sky radiative fluxes. The cloud masking correction is necessary because CRE includes differences between all-sky and clear-sky non-cloud radiative changes, which are not actual cloud radiative responses (Soden et al., 2004). Here  $d\text{CRE}$  is estimated using the TOA CERES EBAF radiative fluxes. The  $dR_x$  terms are diagnosed using all-sky and clear-sky radiative kernels as described above.

The ultimate goal of this study is to derive the IRF from these radiative kernel calculations. Under clear-sky conditions, we simply diagnose  $\text{IRF}^{\text{CS}}$  by rearranging Equation 3, whereby:

$$\text{IRF}^{\text{CS}} = dR^{\text{CS}} - dR_{\lambda}^{\text{CS}} = dR^{\text{CS}} - \left( dR_T^{\text{CS}} + dR_q^{\text{CS}} + dR_{\alpha}^{\text{CS}} \right). \quad (7)$$

For all-sky conditions, an analogous calculation would require  $dR_C$  to be removed from  $dR$ , but since estimating  $dR_C$  as in Equation 6 requires the IRF to be known, this differencing technique is not possible. Following common practice (Soden et al., 2008; Vial et al., 2013), we estimate the all-sky IRF as:

$$\text{IRF} = \frac{\text{IRF}^{\text{CS}}}{\text{Cl}}, \quad (8)$$

where Cl is a constant that accounts for cloud masking of the IRF. For the LW Cl, we use a constant of 1.24, derived by dividing clear-sky and all-sky double-call radiative transfer calculations of  $\text{CO}_2$  IRF from models (Smith et al., 2018). The cloud mask for the shortwave (SW) is derived from direct output of aerosol IRF from Modern-Era Retrospective Analysis for Research and Applications, Version 2 (MERRA-2) reanalysis (Gelaro et al., 2017). The global-mean value is 2.43, in line with a range of observational-based cloud masking estimates by Bellouin et al. (2020). Only the MERRA-2 SW Cl is available over time, but it has an insignificant long-term trend. Consequently, SW IRF has nearly identical trends when computed with a time resolved versus constant SW Cl.

This conversion to all-sky conditions accounts for the presence of clouds but not cloud changes. Therefore, the IRF in this study does not include aerosol-cloud interactions, such as cloud albedo effects (Boucher et al., 2013). Instead, these terms are included in  $dR_C$ . Therefore, the aerosol component to the kernel-derived estimates of IRF is akin to aerosol direct radiative effects found throughout the literature (e.g., Thorsen et al., 2020).

The AIRS L3 data has the shortest record among satellite observations used in this study, with 2003 being the first complete year of data. Thus, we compute all deseasonalized anomalies from 2003 to 2018 relative to the mean of that time span. While we refer to the resulting calculation as the IRF for brevity, we actually show anomalies of the IRF. For comparison, we also estimate the IRF by applying the CloudSat radiative kernels to MERRA-2 reanalysis over the same period. This reanalysis product assimilates a variety of satellite observations, including observations of aerosol properties.

In climate models, idealized simulations and flux diagnostics from double-call radiative transfer calculations can be used to evaluate the accuracy of radiative kernel estimates of  $dR_{\lambda}$  and IRF (e.g., Smith et al., 2018; Vial et al., 2013). Such a comparison is not possible in the observed record or the MERRA-2 reanalysis, however. Since the IRF is derived from differencing the other radiative terms, there will always be near-perfect energy closure, albeit with some error due to cloud masking assumptions, which is typically small (Chung & Soden, 2015). Alternatively, we will compare these kernel-derived estimates to various independent measures of the IRF.

To verify the aerosol component of the IRF, we compare radiative kernel-derived SW IRF to direct output of the aerosol direct radiative effect from MERRA-2. We also compare SW IRF to trends in aerosol optical depth (AOD) from MERRA-2 and observations from the Moderate Resolution Imaging Spectroradiometer (MODIS) merged Dark Target and Deep Blue product (Sayer et al., 2014).

We compare radiative-kernel derived estimates of the LW IRF to offline radiative transfer calculations of GHG IRF. We apply empirical formulas to observed global-mean concentrations of 5 major greenhouse gases ( $\text{CO}_2$ ,  $\text{CH}_4$ ,  $\text{N}_2\text{O}$ , CFC-11, and CFC-12), provided by NOAA Global Monitoring Division (Hoffman et al., 2006; Montzka et al., 2011). Etminan et al. (2016) derive the empirical formulas from polynomial fits to line-by-line radiative forcing calculations. While these formulas were originally developed for net stratospherically adjusted radiative forcing, we use corrections from additional line-by-line calculations (Etminan et al., 2016; Hodnebrog et al., 2013) to calculate TOA IRF, decomposed into a LW and SW component.

We also estimate GHG IRF using the SOCRATES offline radiative transfer model (Edwards et al., 1996; Manners et al., 2015) with NOAA GHG concentrations and atmospheric profiles from the MERRA-2 reanalysis. Like the other IRF estimates, these calculations are presented in anomaly space with the seasonal cycle removed. The IRF from CFCs has decreased recently, but this has been compensated for by a near equal increase from other halocarbons not considered in empirical fit and SOCRATES calculations (Myhre et al., 2013). To account for this, we repeat these calculations with no CFC trend. This only modifies total GHG IRF trends by  $<5\%$ , however, so hereafter we focus on results without this assumption. The SOCRATES IRF calculations are conducted under pristine, clear-sky conditions and converted to all-sky via Equation 8, like the radiative kernel calculations.

The various inputs and assumptions detailed above can contribute uncertainty to the estimated radiative changes. In a supporting Appendix, we provide a comprehensive uncertainty assessment in the IRF trends due to these contributors, including from observed  $dR$ , radiative kernels, and the cloud masking constant,  $Cl$ . We find these uncertainties are smaller than the trend regression uncertainty associated with timeseries variability. Therefore, all trends presented hereafter are provided with 95% confidence intervals (or roughly 2 standard errors around the mean) associated with the least squares linear regression. This is common practice when diagnosing CERES trends (e.g., Loeb et al., 2018a; Loeb et al., 2018b).

The anomalies of  $dR$ ,  $dR_{\lambda}$ , and the IRF are subject to the same sources of uncertainty as long-term trends. Therefore, Figures 1 and 2 below include uncertainty bounds diagnosed as  $2\sigma$  across multiple estimates of the radiative terms using different radiative flux data products from CERES and alternative radiative kernel sets and model estimates of  $Cl$  (see Appendix S1).

### 3. Results

Figure 1a shows a timeseries of global-mean total radiative flux anomalies ( $dR$ ) from CERES satellite observations and its component from radiative responses ( $dR_{\lambda}$ ), estimated by applying the CloudSat-based radiative kernels to CERES and AIRS observations (hereafter CERES/AIRS). Positive anomalies indicate a net increase in downwelling radiation at the TOA (planetary warming). The sum of the radiative responses,  $dR_{\lambda}$ ,

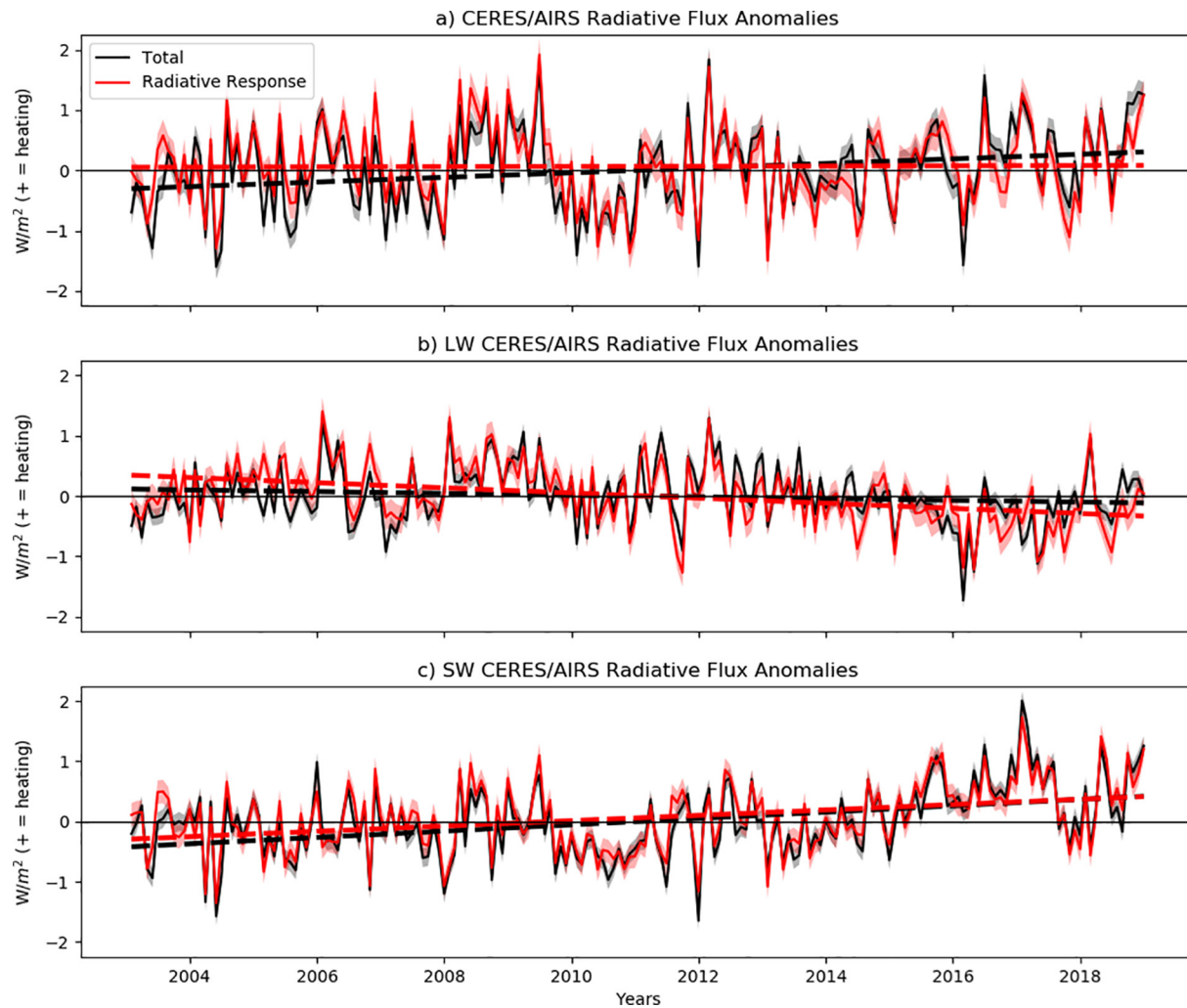


**Figure 1.** Global-mean (a) net, (b) longwave (LW), and (c) shortwave (SW) total radiative flux anomalies from 2003 to 2018 as measured by CERES (black) and the contribution to that total from the sum of radiative responses (red). Respective trendlines are displayed as dashed lines. Uncertainty of  $\pm 2\sigma$  is shown for each timeseries, computed as described in the Methods. Linear trends and 95% confidence intervals are provided in text. CERES, Clouds and Earth's Radiant Energy System.

accounts for nearly all of the total short-term  $dR$  variability, as evident by their strong correlation ( $r = 0.88$ ) and small root-mean-squared difference of  $0.024 \pm 0.003 \text{ W/m}^2$ ;  $\sim 3.5\%$  of the standard deviation of  $dR$ . On inter-annual timescales, ENSO strongly influences this variability (Trenberth et al., 2014), which lags by  $\sim 5$  months (Figure S1; Loeb et al., 2018). Long-term  $dR$  exhibits a positive, linear trend ( $0.038 \pm 0.02 \text{ W/m}^2/\text{year}$ ) significant with 95% confidence, while  $dR_\lambda$  exhibits an insignificant trend ( $0.002 \pm 0.02 \text{ W/m}^2/\text{year}$ ) an order of magnitude smaller. This arises from cancelation between LW and SW  $dR_\lambda$ . The LW  $dR_\lambda$  has a negative linear trend ( $-0.042 \pm 0.02 \text{ W/m}^2/\text{year}$ ) (Figure 1b), mainly from global warming-driven  $dR_T$  decreases ( $-0.041 \pm 0.007 \text{ W/m}^2/\text{year}$ ) (Figure S2). The SW  $dR_\lambda$  trend ( $0.044 \pm 0.02 \text{ W/m}^2/\text{year}$ ) is nearly equal and opposite of the LW, driven by increases in SW  $dR_c$  ( $0.023 \pm 0.09 \text{ W/m}^2/\text{year}$ ) and SW  $dR_C$  ( $0.020 \pm 0.13 \text{ W/m}^2/\text{year}$ ), a predominantly low cloud response (Loeb et al., 2018). The latter alone accounts for most of the SW interannual variability.

MERRA-2 also exhibits a significant, positive trend in  $dR$  but not  $dR_\lambda$  due to compensating LW and SW components (Figure S3). However, there is a positive trend in LW  $dR_\lambda$  and a negative trend in SW  $dR_\lambda$ , opposite from the CERES/AIRS response. This occurs due to a considerably different LW and SW  $dR_C$  (Figure S4) compared to satellite observations.

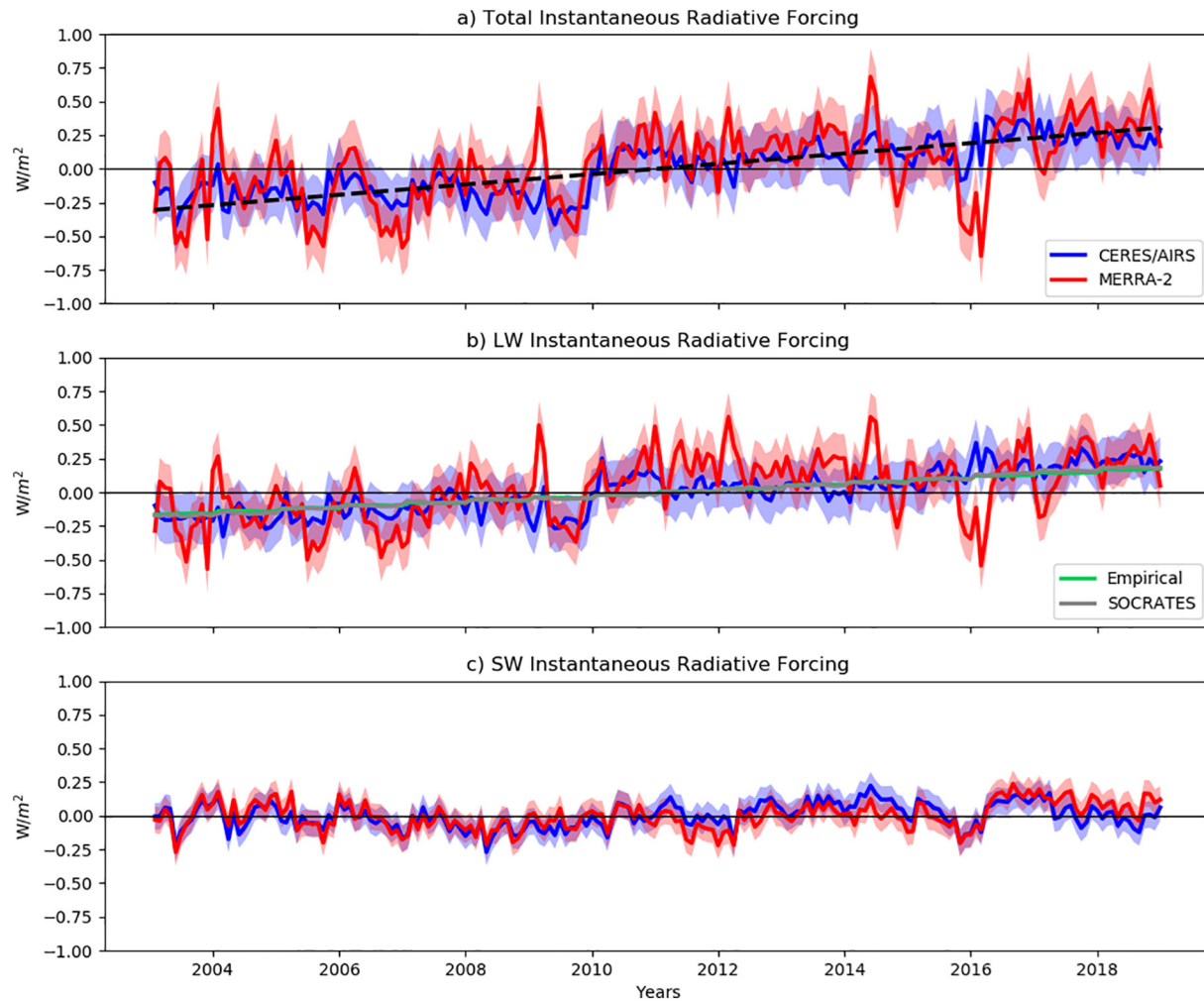


**Figure 2.** Global-mean (a) total, (b) longwave (LW), and (c) shortwave (SW) instantaneous radiative forcing (IRF) estimated from the radiative kernel technique for CERES/AIRS (red) and MERRA-2 (blue). Additional calculations of greenhouse gas-only IRF are also shown using empirical formulas (green) and the SOCRATES radiative transfer model (gray). For reference, the trendline for total radiative flux anomalies (Figure 1a) is displayed with the total IRF as a black dashed line. Uncertainty of  $\pm 2\sigma$  is shown with shading for each timeseries, computed as described in the Methods. Linear trends and 95% confidence intervals are provided in text and in Table 1. CERES, Clouds and Earth's Radiant Energy System; MERRA, Modern-Era Retrospective Analysis for Research and Applications, Version 2.

Since neither  $dR_\lambda$  or its uncertainties account for the positive  $dR$  trend, it must be explained by the IRF. Figure 2 shows the timeseries of the total, LW and SW IRF under all-sky conditions, estimated from the radiative kernel technique. The total CERES/AIRS IRF exhibits a significant, positive trend ( $0.033 \pm 0.007$  W/m<sup>2</sup>/year), mostly from increasing LW IRF ( $0.027 \pm 0.006$  W/m<sup>2</sup>/year). The SW IRF exhibits a smaller, yet still significant increase ( $0.006 \pm 0.003$  W/m<sup>2</sup>/year). The LW IRF trend is opposite in sign from LW  $dR$ , since decreasing LW  $dR_\lambda$  compensates. In the SW, IRF and  $dR$  are both increasing, but SW  $dR_\lambda$  is the dominant contributor while the IRF trend is much smaller.

Rising GHG concentrations explain the positive LW IRF trend. Accordingly, it increases at a similar rate to the GHG IRF estimates from the empirical fit ( $0.021 \pm 0.0002$  W/m<sup>2</sup>/year or  $0.022 \pm 0.0002$  W/m<sup>2</sup>/year if ignoring CFCs [see Methods]) and the SOCRATES radiative transfer model ( $0.023 \pm 0.0003$  W/m<sup>2</sup>/year) (Figure 2b), despite these calculations neglecting some GHG forcers found in nature, such as ozone. MERRA-2 exhibits a similar LW IRF trend to CERES/AIRS ( $0.029 \pm 0.003$  W/m<sup>2</sup>/year) while direct output of the LW aerosol IRF from MERRA-2 exhibits no trend. This further indicates GHG increases account for roughly all LW IRF increases.

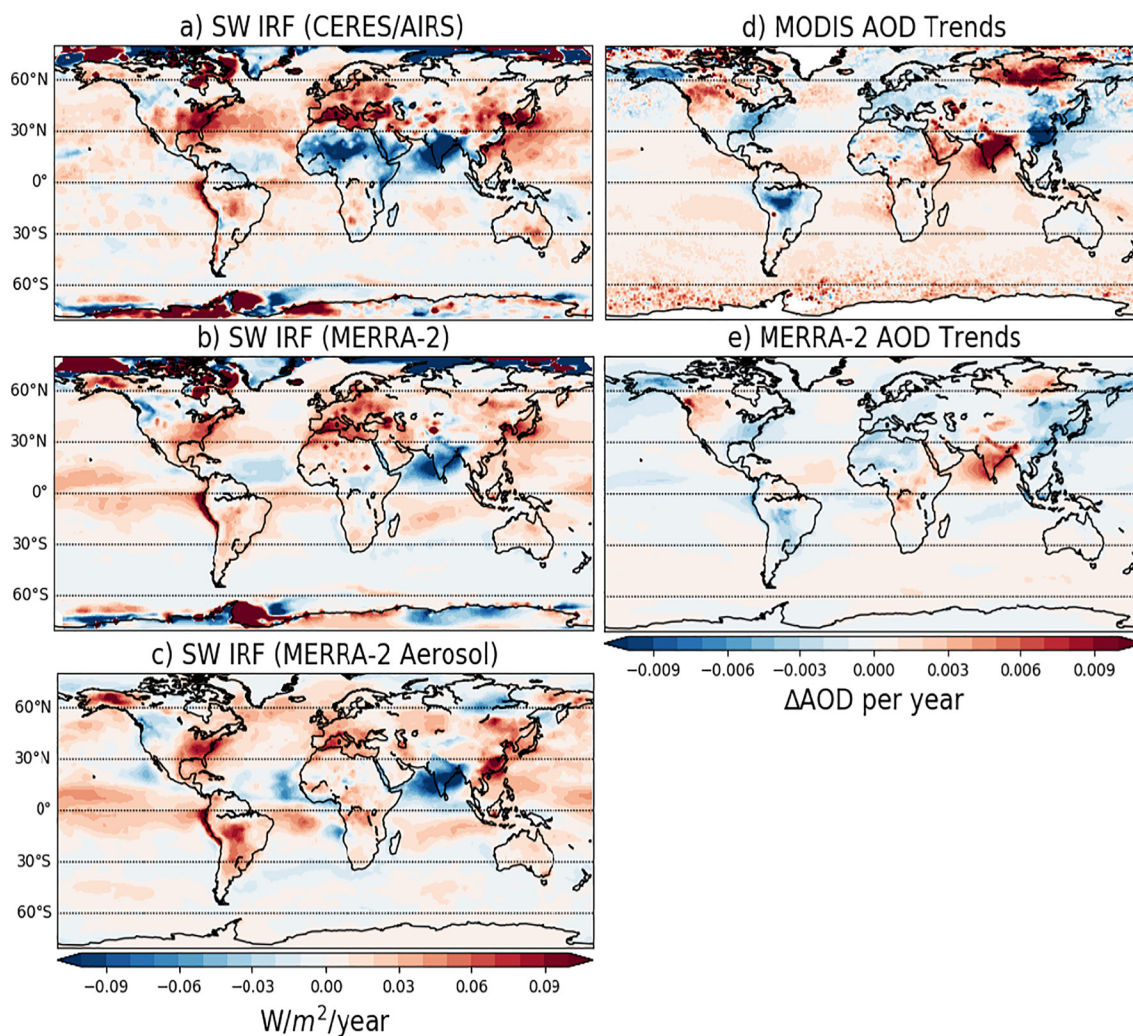


**Figure 3.** Local linear trends from 2003 to 2018 in all-sky shortwave instantaneous radiative forcing (SW IRF) diagnosed in (a) CERES/AIRS observations and (b) MERRA-2 reanalysis using the radiative kernel differencing technique and (c) from direct output of MERRA-2 aerosol IRF. Also, local linear trends over the same time period are shown for aerosol optical depth (AOD) from (d) MODIS and (e) MERRA-2. CERES, Clouds and Earth's Radiant Energy System; IRF, instantaneous radiative forcing; MERRA, Modern-Era Retrospective Analysis for Research and Applications, Version 2; SW, shortwave (SW).

Increasing GHG concentrations also contribute ( $0.002 \pm 0.00$   $W/m^2/year$ ) to the total positive SW IRF trends, according to estimates from the empirical fits. The SW GHG trend is negligible in the SOCRATES calculations, but the model version used here does not account for the SW absorption of  $CH_4$ .

The total SW IRF increase is nearly identical in CERES/AIRS and MERRA-2, and to aerosol-only SW IRF trends from MERRA-2 direct output (Figure S5). They also exhibit similar short-term variability. This suggests aerosols explain most of the SW IRF. The long-term radiative heating is consistent with declining anthropogenic aerosol emissions during this period (Q. Zhang et al., 2019). Toward the end of the timeseries, CERES/AIRS SW IRF has more positive anomalies than the SW IRF from MERRA-2. Locally, the largest differences with MERRA-2 after 2015 are in major absorbing aerosol source regions (Figure S6), suggesting a contribution from different absorbing aerosol properties.

Figure 3 shows local linear trends in kernel-derived, total SW IRF from CERES/AIRS and MERRA-2 and direct MERRA-2 output of aerosol-only SW IRF (Figure 3c). The spatial pattern of the SW IRF trend is generally consistent across all three estimates. A notable hemispheric asymmetry is present, with large changes concentrated in the populous Northern Hemisphere. This includes large positive trends over the Eastern United States, Western Europe, and Eastern China, where anthropogenic emissions of reflective

aerosols have declined because of government actions to combat poor air quality (Kühn et al., 2014; Ridley et al., 2018; Q. Zhang et al., 2019). In contrast, the SW IRF trends are negative over India, where emissions continue to rise (Dey et al., 2012).

There are some magnitude differences in these major source regions, however. For instance, trends are larger in the Eastern US and India in CERES/AIRS than in MERRA-2. This coincides with differences in the MODIS and MERRA-2 AOD trends (Figure 3d and 3e), which are also larger in MODIS. Over Saharan Africa, the sign of the SW IRF trend differs, consistent with opposing trends in MODIS and MERRA-2 AOD. Dust radiative forcing during this period is likely a key factor (Figure S7; Shao et al., 2013) and is highly uncertain (Kok et al., 2017; Miller et al., 2014).

The strong agreement in MERRA-2 trends from kernel differencing versus direct SW aerosol IRF output (Figure 3b and 3c) highlights the dominant role of aerosols in the total SW IRF trends. It also confirms the accuracy of the radiative kernel technique. The kernel differencing method results in artifacts in the polar regions, however, where large local trends are a consequence of underestimating the SW  $dR_{\alpha}$  removed from  $dR$  (Figure S8) and not from actual forcing. One possible explanation is surface albedo radiative kernels fail to capture important ice-albedo feedback non-linearities (Block & Mauritsen, 2013). Nevertheless, the polar region errors have negligible effect on global-mean SW IRF trends.

Some inter- and intra-annual variability (hereafter short-term variability) in SW IRF is expected, given natural variations in aerosol concentrations. Consequently, the detrended aerosol-only ( $\sigma = 0.088 \text{ W/m}^2$ ) and kernel-derived ( $\sigma = 0.097 \text{ W/m}^2$ ) SW IRF in MERRA-2 exhibit similar variability and are highly correlated ( $r = 0.78$ ). The source of the notable short-term variability in LW IRF (Figure 2b) is less apparent, however, since greenhouse gas concentrations increase relatively steadily on these timescales, as evident in the empirical fit estimate of GHG IRF, which increases almost perfectly linearly.

While radiative kernel error may play some role, the LW IRF from CERES/AIRS exhibits considerably more short-term variability ( $\sigma = 0.24$ ) than MERRA-2 ( $\sigma = 0.16$ ), despite using the same CloudSat-derived radiative kernels in both estimates. This highlights short-term inconsistencies between the radiative fluxes observed by CERES ( $dR^{\text{CS}}$ ) and the AIRS retrievals used to diagnose LW  $dR_{\lambda}^{\text{CS}}$ . For instance, the difference between CERES/AIRS and MERRA-2  $dR_{\lambda}^{\text{CS}}$  exhibits considerably more short-term variability than the difference between  $dR^{\text{CS}}$ . This is mostly due to different variability in  $dR_T^{\text{CS}}$  (Figure S9), and more specifically due to different temperature anomalies at the surface and in the boundary layer between AIRS and MERRA-2 (Figure S10). Since AIRS temperature anomalies are more variable, so is the  $dR_T^{\text{CS}}$  estimate. And since this variability is not also observed radiatively by CERES, it is not evident in  $dR^{\text{CS}}$ . This ultimately translates to a more variable LW IRF when using the kernel differencing technique. This also explains why LW IRF spatial patterns are noisier for CERES/AIRS than for MERRA-2 (Figure S11). Cloud contamination likely contributes to the AIRS temperature variability, as found previously (Hearty et al., 2014). This is evident at the surface, for example, where the largest differences between AIRS and MERRA-2 temperature anomalies tend to occur where clouds are common (Figure S9), especially over land. While global-mean surface temperature anomalies from AIRS closely agree with other, independent datasets (Susskind et al., 2019), it is possible the temperature biases that do exist are magnified in the context of radiative changes.

The LW IRF variability may also stem from its sensitivity to the atmospheric base state (Pincus et al., 2015). However, this contribution appears to be small. In the LW GHG IRF estimated from the SOCRATES radiative transfer model, we use daily MERRA-2 temperature, surface albedo and humidity data, thus capturing the GHG IRF sensitivity to the unperturbed, non-cloud base state. Still, the short-term variability from this offline calculation is nearly as small as estimates with the empirical fit, which does not account for base state variability. The LW IRF short-term variability in this comparison (and in the radiative kernel-derived estimates) is not due to variations in the cloud base state since LW cloud masking is always treated as a constant. While clouds may play a greater role in reality, the SW IRF estimated from radiative kernels with constant cloud masking has similar short-term variability to the aerosol-only SW IRF in MERRA-2, which accounts for cloud masking temporal variations. This suggests cloud variability may not be important in the global-mean. Lastly, some LW IRF variability in MERRA-2 (and in CERES/AIRS) may be due to spatial variability in the GHG concentrations (Myhre et al., 2013), which is not present in the empirical fit or the SOCRATES estimates.



**Table 1**  
Global-Mean Linear Trends ( $W/m^2/year$ )

	LW	SW	Net
CERES/AIRS	$0.027 \pm 0.006$	$0.006 \pm 0.003$	$0.033 \pm 0.007$
MERRA-2	$0.029 \pm 0.003$	$0.006 \pm 0.003$	$0.035 \pm 0.004$
Aerosol-Only MERRA-2	$-4.2E-4 \pm 1.5E-4$	$0.006 \pm 0.003$	$0.006 \pm 0.003$

Note. 95% confidence bounds in instantaneous radiative forcing estimated using the radiative kernel differencing technique (first two rows) and MERRA-2 flux diagnostics (third row).

LW, longwave; SW, shortwave.

## 4. Conclusions

We have diagnosed the global IRF directly from observations using radiative kernels. Table 1 summarizes linear trends. We find that from 2003 to 2018, the observed IRF has increased  $0.53 \pm 0.11 W/m^2$ , almost entirely accounting for the positive trend in CERES TOA radiative flux anomalies ( $dR$ ). The intrinsic LW and SW climate radiative responses largely cancel out. This IRF increase mostly occurs in the LW ( $0.43 \pm 0.1 W/m^2$ ), driven by rising greenhouse gas concentrations. This serves as direct observational evidence that anthropogenic activity is impacting the Earth's energy balance. The SW IRF has also increased ( $0.1 \pm 0.05 W/m^2$ ). In part, this is a reflection of government-mandated aerosol emission reductions throughout major source regions, which may have a greater direct impact than inferred by the SW IRF, which does not include aerosol cloud-albedo effects in this analysis.

Diagnosing the observed IRF is important for our fundamental understanding of Earth's response to climate change and a valuable piece of information for policy decisions. Conceivably, observed IRF could be used as a top-down approach for monitoring the climate response to mitigation efforts. By applying published metrics of instrumental uncertainty in AIRS (Hearty et al., 2014; Tobin et al., 2006) and CERES (Loeb et al., 2018b), along with the kernel-derived IRF variance and trend, we apply formulas by Leroy et al. (2008) to determine the minimum length of the observational record necessary to detect a climate change signal. These formulas account for trend uncertainty due to natural variability and instrumental uncertainty. Using this approach, we find total IRF trends are detectable, given these sources of uncertainty, within 3.8 years using the satellite data presented in this study. Therefore, the methods introduced here could be useful for near-real time monitoring, especially since the time to detection shortens with the lengthening of the observational record.

## Conflicts of Interest

The authors declare no conflicts of interest relevant to this study.

## Data Availability Statement

The CERES radiative flux observations are available at <https://ceres.larc.nasa.gov/data/>. The AIRS temperature and water vapor observations and the MERRA-2 reanalysis data are available at <https://disc.gsfc.nasa.gov/>. The CloudSat/CALIPSO radiative kernels used in this study and related code for applying them are available at <https://climate.rsmas.miami.edu/data/radiative-kernels/>.

## References

- Aumann, H. H., Chahine, M. T., Gautier, C., Goldberg, M. D., Kalnay, E., McMillin, L. M., et al. (2003). AIRS/AMSU/HSB on the Aqua mission: Design, science objectives, data products, and processing systems. *IEEE Transactions on Geoscience and Remote Sensing*, 41(2), 253–264. <https://doi.org/10.1109/TGRS.2002.808356>
- Bellouin, N., Quaas, J., Gryspeerdt, E., Kinne, S., Stier, P., Watson-Parris, D., et al. (2020). Bounding global aerosol radiative forcing of climate change. *Reviews of Geophysics*, 58(1), e2019RG000660. <https://doi.org/10.1029/2019RG000660>
- Block, K., & Mauritsen, T. (2013). Forcing and feedback in the MPI-ESM-LR coupled model under abruptly quadrupled CO<sub>2</sub>. *Journal of Advances in Modeling Earth Systems*, 5(4), 676–691. <https://doi.org/10.1002/jame.20041>

## Acknowledgments

The authors thank the Editor, reviewers and Graeme Stephens for valuable feedback on this work. R. J. Kramer is supported by an appointment to the NASA Postdoctoral Program administered by Universities Space Research Association. HH and BJS are supported by NASA award 80NSSC18K1032. L. Oreopoulos gratefully acknowledges support from NASA's CloudSat/CALIPSO Science Team and MEaSUREs programs. G. Myhre, P. M. Forster and C. J. Smith were supported by European Union's Horizon 2020 Research and Innovation Programme under grant agreement no. 820829 (CONSTRIN). P. M. Forster and C. J. Smith were also supported by UKRI NERC grant NE/N006038/1 (SMURPHS). C. J. Smith was supported by a NERC/IIASA Collaborative Research Fellowship (NE/T009381/1).

- Bony, S., Semie, A., Kramer, R. J., Soden, B., Tompkins, A. M., & Emanuel, K. A. (2020). Observed modulation of the tropical radiation budget by deep convective organization and lower-tropospheric stability. *AGU Advances*, 1(3), e2019AV000155. <https://doi.org/10.1029/2019AV000155>
- Boucher, O., Randall, D., Artaxo, P., Bretherton, C., Feingold, G., Forster, P., et al. (2013). Clouds and aerosols. In T. F. Stocker, D. Qin, G.-K. Plattner, M. Tignor, S. K. Allen, J. Doschung, et al. (Eds.), *Climate change 2013: The physical science basis. Contribution of working group I to the fifth assessment report of the intergovernmental panel on climate change* (pp. 571–657). Cambridge University Press. <https://doi.org/10.1017/CBO9781107415324.016>
- Chung, E.-S., & Soden, B. J. (2015). An assessment of direct radiative forcing, radiative adjustments, and radiative feedbacks in coupled ocean-atmosphere models. *Journal of Climate*, 28(10), 4152–4170. <https://doi.org/10.1175/JCLI-D-14-00436.1>
- Collins, W. D., Ramaswamy, V., Schwarzkopf, M. D., Sun, Y., Portmann, R. W., Fu, Q., et al. (2006). Radiative forcing by well-mixed greenhouse gases: Estimates from climate models in the intergovernmental panel on climate change (IPCC) fourth assessment report (AR4). *Journal of Geophysical Research*, 111(D14), D14317. <https://doi.org/10.1029/2005JD006713>
- Dey, S., Di Girolamo, L., van Donkelaar, A., Tripathi, S. N., Gupta, T., & Mohan, M. (2012). Variability of outdoor fine particulate (PM<sub>2.5</sub>) concentration in the Indian Subcontinent: A remote sensing approach. *Remote Sensing of Environment*, 127, 153–161. <https://doi.org/10.1016/j.rse.2012.08.021>
- Edwards, J. M., & Slingo, A. (1996). Studies with a flexible new radiation code. I: Choosing a configuration for a large-scale model. *Quarterly Journal of the Royal Meteorological Society*, 122(531), 689–719. <https://doi.org/10.1002/qj.49712253107>
- Etminan, M., Myhre, G., Highwood, E. J., & Shine, K. P. (2016). Radiative forcing of carbon dioxide, methane, and nitrous oxide: A significant revision of the methane radiative forcing. *Geophysical Research Letters*, 43(24), 12614–12623. <https://doi.org/10.1002/2016GL071930>
- Feldman, D. R., Collins, W. D., Gero, P. J., Torn, M. S., Mlawer, E. J., & Shippert, T. R. (2015). Observational determination of surface radiative forcing by CO<sub>2</sub> from 2000 to 2010. *Nature*, 519(7543), 339–343. <https://doi.org/10.1038/nature14240>
- Feldman, D. R., Collins, W. D., Biraud, S. C., Risser, M. D., Turner, D. D., Gero, P. J., et al. (2018). Observationally derived rise in methane surface forcing mediated by water vapour trends. *Nature Geoscience*, 11(4), 238–243. <https://doi.org/10.1038/s41561-018-0085-9>
- Friedlingstein, P., Jones, M. W., O'Sullivan, M., Andrew, R. M., Hauck, J., Peters, G. P., et al. (2019). Global carbon budget 2019. *Earth System Science Data*, 11(4), 1783–1838. <https://doi.org/10.5194/essd-11-1783-2019>
- Gelaro, R., McCarty, W., Suárez, M. J., Todling, R., Molod, A., Takacs, L., et al. (2017). The modern-era retrospective analysis for research and applications, version 2 (MERRA-2). *Journal of Climate*, 30(14), 5419–5454. <https://doi.org/10.1175/JCLI-D-16-0758.1>
- Harries, J. E., Brindley, H. E., Sagoo, P. J., & Bantges, R. J. (2001). Increases in greenhouse forcing inferred from the outgoing longwave radiation spectra of the Earth in 1970 and 1997. *Nature*, 410(6826), 355–357. <https://doi.org/10.1038/35066553>
- Hearty, T. J., Savtchenko, A., Tian, B., Fetzer, E., Yung, Y. L., Theobald, M., et al. (2014). Estimating sampling biases and measurement uncertainties of AIRS/AMSU-A temperature and water vapor observations using MERRA reanalysis. *Journal of Geophysical Research: Atmospheres*, 119(6), 2725–2741. <https://doi.org/10.1002/2013JD021205>
- Hodnebrog, Ø., Etminan, M., Fuglestedt, J. S., Marston, G., Myhre, G., Nielsen, C. J., et al. (2013). Global warming potentials and radiative efficiencies of halocarbons and related compounds: A comprehensive review. *Reviews of Geophysics*, 51(2), 300–378. <https://doi.org/10.1002/rog.20013>
- Hofmann, D. J., Butler, J. H., Dlugokencky, E. J., Elkins, J. W., Masarie, K., Montzka, S. A., & Tans, P. (2006). The role of carbon dioxide in climate forcing from 1979 to 2004: Introduction of the annual greenhouse gas index. *Tellus B: Chemical and Physical Meteorology*, 58(5), 614–619. <https://doi.org/10.1111/j.1600-0889.2006.00201.x>
- Jiang, Y., Aumann, H. H., Wingyee-Lau, M., & Yung, Y. L. (2011). *Climate change sensitivity evaluation from AIRS and IRIS measurements*. In Earth Observing Systems XVI (Vol. 8153, p. 81531Z). Proceedings of SPIE. International Society for Optics and Photonics. <http://dx.doi.org/10.1117/12.892817>
- Kato, S., Rose, F. G., Rutan, D. A., Thorsen, T. J., Loeb, N. G., Doelling, D. R., et al. (2018). Surface irradiances of edition 4.0 clouds and the Earth's radiant energy system (CERES) energy balanced and filled (EBAF) data product. *Journal of Climate*, 31(11), 4501–4527. <https://doi.org/10.1175/JCLI-D-17-0523.1>
- Kok, J. F., Ridley, D. A., Zhou, Q., Miller, R. L., Zhao, C., Heald, C. L., et al. (2017). Smaller desert dust cooling effect estimated from analysis of dust size and abundance. *Nature Geoscience*, 10(4), 274–278. <https://doi.org/10.1038/ngeo2912>
- Kramer, R. J., Matus, A. V., Soden, B. J., & L'Ecuyer, T. S. (2019). Observation-based radiative kernels from CloudSat/CALIPSO. *Journal of Geophysical Research: Atmosphere*, 124(10), 5431–5444. <https://doi.org/10.1029/2018JD029021>
- Kühn, T., Partanen, A.-I., Laakso, A., Lu, Z., Bergman, T., Mikkonen, S., et al. (2014). Climate impacts of changing aerosol emissions since 1996. *Geophysical Research Letters*, 41(13), 4711–4718. <https://doi.org/10.1002/2014GL060349>
- Leroy, S. S., Anderson, J. G., & Ohring, G. (2008). Climate signal detection times and constraints on climate benchmark accuracy requirements. *Journal of Climate*, 21, 841–846. <https://doi.org/10.1175/2007jcli1946.1>
- Loeb, N., Thorsen, T., Norris, J., Wang, H., & Su, W. (2018a). Changes in earth's energy budget during and after the "Pause" in global warming: An observational perspective. *Climate*, 6, 62. <https://doi.org/10.3390/cli6030062>
- Loeb, N. G., Doelling, D. R., Wang, H., Su, W., Nguyen, C., Corbett, J. G., et al. (2018b). Clouds and the Earth's radiant energy system (CERES) energy balanced and filled (EBAF) top-of-atmosphere (TOA) edition-4.0 data product. *Journal of Climate*, 31(2), 895–918. <https://doi.org/10.1175/JCLI-D-17-0208.1>
- Loeb, N. G., Rose, F. G., Kato, S., Rutan, D. A., Su, W., Wang, H., et al. (2019). Toward a consistent definition between satellite and model clear-sky radiative fluxes. *Journal of Climate*, 33(1), 61–75. <https://doi.org/10.1175/JCLI-D-19-0381.1>
- Manners, J., Edwards, J. M., Hill, P., & Thelen, J.-C. (2015). *SOCRATES (Suite Of Community Radiative Transfer codes based on Edwards and Slingo) technical guide*. Met Office
- Miller, R. L., Knippertz, P., Pérez García-Pando, C., Perlwitz, J. P., & Tegen, I. (2014). Impact of dust radiative forcing upon climate. In P. Knippertz, & J.-B. W. Stuut (Eds.), *Mineral dust: A key player in the Earth system* (pp. 327–357). Dordrecht: Springer. Retrieved from [https://doi.org/10.1007/978-94-017-8978-3\\_13](https://doi.org/10.1007/978-94-017-8978-3_13)
- Mlynczak, M. G., Daniels, T. S., Kratz, D. P., Feldman, D. R., Collins, W. D., Mlawer, E. J., et al. (2016). The spectroscopic foundation of radiative forcing of climate by carbon dioxide. *Geophysical Research Letters*, 43(10), 5318–5325. <https://doi.org/10.1002/2016GL068837>
- Montzka, S. A., Dlugokencky, E. J., & Butler, J. H. (2011). Non-CO<sub>2</sub> greenhouse gases and climate change. *Nature*, 476(7358), 43–50. <https://doi.org/10.1038/nature10322>
- Myhre, G., Shindell, D., Bréon, F.-M., Collins, W., Fuglestedt, J., Huang, J., et al. (2013). Anthropogenic and natural radiative forcing. In T. F. Stocker, D. Qin, G.-K. Plattner, M. Tignor, S. K. Allen, J. Doschung, et al. (Eds.), *Climate change 2013: The physical science basis. Contribution of working group I to the fifth assessment report of the intergovernmental panel on climate change* (pp. 659–740). Cambridge University Press. <https://doi.org/10.1017/CBO9781107415324.018>

Pendergrass, A. G., Conley, A., & Vitt, F. M. (2018). Surface and top-of-atmosphere radiative feedback kernels for CESM-CAM5. *Earth System Science Data*, 10(1), 317–324. <https://doi.org/10.5194/essd-10-317-2018>

Philipona, R., Dürr, B., Marty, C., Ohmura, A., & Wild, M. (2004). Radiative forcing—measured at Earth’s surface—corroborate the increasing greenhouse effect. *Geophysical Research Letters*, 31(3). <https://doi.org/10.1029/2003GL018765>

Pincus, R., Buehler, S. A., Brath, M., Jamil, O., Evans, F., Manners, J., et al. (2020). Benchmark calculations of radiative forcing by greenhouse gases. *Earth and Space Science Open Archive*, 15. <https://doi.org/10.1002/essoar.10501550.1>

Pincus, R., Mlawer, E. J., Oreopoulos, L., Ackerman, A. S., Baek, S., Brath, M., et al. (2015). Radiative flux and forcing parameterization error in aerosol-free clear skies. *Geophysical Research Letters*, 42(13), 5485–5492. <https://doi.org/10.1002/2015GL064291>

Raghuraman, S. P., Paynter, D., & Ramaswamy, V. (2019). Quantifying the drivers of the clear sky greenhouse effect, 2000–2016. *Journal of Geophysical Research: Atmospheres*, 124(21), 11354–11371. <https://doi.org/10.1029/2019JD031017>

Randles, C. A., Kinne, S., Myhre, G., Schulz, M., Stier, P., Fischer, J., et al. (2013). Intercomparison of shortwave radiative transfer schemes in global aerosol modeling: Results from the AeroCom radiative transfer experiment. *Atmospheric Chemistry and Physics*, 13(5), 2347–2379. <https://doi.org/10.5194/acp-13-2347-2013>

Ridley, D. A., Heald, C. L., Ridley, K. J., & Kroll, J. H. (2018). Causes and consequences of decreasing atmospheric organic aerosol in the United States. *Proceedings of the National Academy of Sciences of the United States of America*, 115(2), 290. <https://doi.org/10.1073/pnas.1700387115>

Sayer, A. M., Munchak, L. A., Hsu, N. C., Levy, R. C., Bettenhausen, C., & Jeong, M.-J. (2014). MODIS Collection 6 aerosol products: Comparison between Aqua’s e-deep blue, dark target, and “merged” data sets, and usage recommendations. *Journal of Geophysical Research: Atmosphere*, 119(24), 13965–13989. <https://doi.org/10.1002/2014JD022453>

Shao, Y., Klose, M., & Wyrwoll, K.-H. (2013). Recent global dust trend and connections to climate forcing. *Journal of Geophysical Research: Atmosphere*, 118(19), 11107–11118. <https://doi.org/10.1002/jgrd.50836>

Sherwood, S. C., Bony, S., Boucher, O., Bretherton, C., Forster, P. M., Gregory, J. M., & Stevens, B. (2015). Adjustments in the forcing-feedback framework for understanding climate change. *Bulletin of the American Meteorological Society*, 96(2), 217–228. <https://doi.org/10.1175/BAMS-D-13-00167.1>

Smith, C. J., Kramer, R. J., Myhre, G., Forster, P. M., Soden, B. J., Andrews, T., et al. (2018). Understanding rapid adjustments to diverse forcing agents. *Geophysical Research Letters*, 45(21), 12023–12031. <https://doi.org/10.1029/2018GL079826>

Soden, B. J., Broccoli, A. J., & Hemler, R. S. (2004). On the use of cloud forcing to estimate cloud feedback. *Journal of Climate*, 17(19), 3661–3665. [https://doi.org/10.1175/1520-0442\(2004\)017<3661:OTUOCF>2.0.CO;2](https://doi.org/10.1175/1520-0442(2004)017<3661:OTUOCF>2.0.CO;2)

Soden, B. J., Collins, W. D., & Feldman, D. R. (2018). Reducing uncertainties in climate models. *Science*, 361(6400), 326–327. <https://doi.org/10.1126/science.aau1864>

Soden, B. J., Held, I. M., Colman, R., Shell, K. M., Kiehl, J. T., & Shields, C. A. (2008). Quantifying climate feedbacks using radiative kernels. *Journal of Climate*, 21(14), 3504–3520. <https://doi.org/10.1175/2007JCLI2110.1>

Stier, P., Schutgens, N. A. J., Bellouin, N., Bian, H., Boucher, O., Chin, M., et al. (2013). Host model uncertainties in aerosol radiative forcing estimates: Results from the AeroCom prescribed intercomparison study. *Atmospheric Chemistry and Physics*, 13(6), 3245–3270. <https://doi.org/10.5194/acp-13-3245-2013>

Susskind, J., Schmidt, G. A., Lee, J. N., & Iredell, L. (2019). Recent global warming as confirmed by AIRS. *Environmental Research Letters*, 14(4), 044030. <https://doi.org/10.1088/1748-9326/aafd4e>

Thorsen, T. J., Kato, S., Loeb, N. G., & Rose, F. G. (2018). Observation-based decomposition of radiative perturbations and radiative kernels. *Journal of Climate*, 31(24), 10039–10058. <https://doi.org/10.1175/JCLI-D-18-0045.1>

Thorsen, T. J., Winker, D. M., & Ferrare, R. A. (2020). Uncertainty in observational estimates of the aerosol direct radiative effect and forcing. *Journal of Climate*, 34, 1–63. <https://doi.org/10.1175/JCLI-D-19-1009.1>

Tobin, D. C., Revercomb, H. E., Knuteson, R. O., Lesht, B. M., Strow, L. L., Hannon, S. E., et al. (2006). Atmospheric radiation measurement site atmospheric state best estimates for atmospheric infrared sounder temperature and water vapor retrieval validation. *Journal of Geophysical Research*, 111(D9). <https://doi.org/10.1029/2005JD006103>

Trenberth, K. E., Fasullo, J. T., & Balmaseda, M. A. (2014). Earth’s energy imbalance. *Journal of Climate*, 27(9), 3129–3144. <https://doi.org/10.1175/JCLI-D-13-00294.1>

Trenberth, K. E., Zhang, Y., & Fasullo, J. T. (2015). Relationships among top-of-atmosphere radiation and atmospheric state variables in observations and CESM. *Journal of Geophysical Research: Atmosphere*, 120(19), 10074–10090. <https://doi.org/10.1002/2015JD023381>

Vial, J., Dufresne, J.-L., & Bony, S. (2013). On the interpretation of inter-model spread in CMIP5 climate sensitivity estimates. *Climate Dynamics*, 41(11), 3339–3362. <https://doi.org/10.1007/s00382-013-1725-9>

Watson-Parris, D., Bellouin, N., Deaconu, L. T., Schutgens, N. A. J., Yoshioka, M., Regayre, L. A., et al. (2020). Constraining uncertainty in aerosol direct forcing. *Geophysical Research Letters*, 47(9), e2020GL087141. <https://doi.org/10.1029/2020GL087141>

Zhang, B., Kramer, R. J., & Soden, B. J. (2019). Radiative feedbacks associated with the Madden-Julian oscillation. *Journal of Climate*, 32(20), 7055–7065. <https://doi.org/10.1175/JCLI-D-19-0144.1>

Zhang, Q., Zheng, Y., Tong, D., Shao, M., Wang, S., Zhang, Y., et al. (2019). Drivers of improved PM2.5 air quality in China from 2013 to 2017. *Proceedings of the National Academy of Sciences of the United States of America*, 116(49), 24463–24469. <https://doi.org/10.1073/pnas.1907956116>

## References From the Supporting Information

Myhre, G., Samset, B. H., Schulz, M., Balkanski, Y., Bauer, S., Bernsten, T. K., et al. (2013). Radiative forcing of the direct aerosol effect from AeroCom Phase II simulations. *Atmospheric Chemistry and Physics*, 13(4), 1853–1877. <https://doi.org/10.5194/acp-13-1853-2013>

Smith, C. J., Kramer, R. J., Myhre, G., Alterskjær, K., Collins, W., Sima, A., et al. (2020). Effective radiative forcing and adjustments in CMIP6 models. *Atmospheric Chemistry and Physics*, 20(16), 9591–9618. <https://doi.org/10.5194/acp-20-9591-2020>

Taylor, K., Ronald, S., & Meehl, G. (2012). An overview of CMIP5 and the experiment design. *Bulletin of the American Meteorological Society*, 93, 485–498. <https://doi.org/10.1175/BAMS-D-11-00094.1>